Check for updates

Advanced Functional Materials

ADVANCED FUNCTIONAL MATERIALS
www.afm-journal.de

RESEARCH ARTICLE

Shallow Trap States Control Electrical Performance of Amorphous Oxide Semiconductor Thin-Film Transistors

Måns J. Mattsson[1] | Jinhan Lee[2] | Christopher E. Malmberg[3] | Jared Parker[1] | Kyle T. Vogt[1] | Hyemi Kim[4] | Minji Hong[4] | Pilsang Yun[4] | Daewon Ha[4] | Taeyoon Lee[2] | Paul H.-Y. Cheong[3] | John F. Wager[5] | Matt W. Graham[1]

[1]Department of Physics, Oregon State University, Corvallis, Oregon, USA | [2]School of Electrical and Electronic Engineering, Yonsei University, Seoul, South Korea | [3]Department of Chemistry, Oregon State University, Corvallis, Oregon, USA | [4]Advanced Device Research Lab, Samsung Electronics, Hwaseong-si, Gyeonggi-do, South Korea | [5]School of Electrical Engineering and Computer Science, Oregon State University, Corvallis, Oregon, USA

Correspondence: Måns J. Mattsson (mattssma@oregonstate.edu) | Matt W. Graham (graham@physics.oregonstate.edu)

Received: 3 February 2026 | **Revised:** 4 August 2026 | **Accepted:** 20 August 2026

Keywords: amorphous oxide | defects | density of states | IGZO | transistor modeling

ABSTRACT

The performance of *n*-type amorphous oxide semiconductor thin-film transistors (TFTs) is controlled by the electronic states near the conduction band mobility edge. Here, the full subgap density of states (DoS) of amorphous InGaZnO (a-IGZO) TFTs, used in display panels and dynamic random-access memory (DRAM) development, is measured by ultrabroadband photoconduction (UP-DoS) microscopy to within 0.1 eV of the mobility edge. The measured subgap DoS for 25 TFT processing conditions accurately predicts each transfer curve, showing how shallow defect states are electron traps that rigidly tune subthreshold swing, threshold voltage, and drift mobility. For a set of TFTs, the subthreshold transfer characteristics can be simulated independently by the experimental shallow-defect DoS, with no adjustable parameters. The full transfer curve is simulated by introducing a single parameter: the conduction band tail energy. Additionally, each simulation reveals how the shallow trap density controls subthreshold behavior and can be directly extracted from transfer curves. Finally, a systematic In-enrichment study, combined with DFT+U DoS simulations, enables identification of vacancy-cation coordination environments for experimentally observed subgap peaks. The dominant trap controlling conventional a-IGZO TFT performance is centered at ~0.32 eV below the conduction band mobility edge and is attributed to a Ga-Ga-In oxygen-vacancy defect.

1 | Introduction

Amorphous oxide semiconductors (AOS) are an established active channel material for flat-panel display thin-film transistors (TFTs) [1–4], which are now being developed for next-generation dynamic random access memory (DRAM) [5–7] and neuromorphic computing architectures [8–10]. The amorphous and oxygen-deficient nature of AOS leads to a high concentration of subgap defect states. Since the defect landscape of such TFTs often varies unpredictably with the specific processing and growth conditions, precise defect control remains an unsolved problem for AOS [11–13]. This problem is only amplified for three-dimensional stacked DRAM architectures, where bottom transistors are known to degrade and induce new defects during the processing of subsequent layers [14]. While such subgap defect traps are thought to degrade charge-transport properties, there is no established method for directly measuring the on-chip defect density of states (DoS) to systematically predict the electrical performance of AOS TFTs.

All rights reserved, including rights for text and data mining and training of artificial intelligence technologies or similar technologies.
© 2026 Wiley-VCH GmbH

Amorphous indium gallium zinc oxide (a-IGZO) is an n-type wide-bandgap AOS widely used in display panels and an emerging material for next-generation DRAM architectures needed for the growing data centers and AI computing demands [15–18]. To enable innovations such as AOS DRAM, a-IGZO offers several advantages over traditional single-crystal silicon due to its low processing temperature, low leakage current, and amorphous structure, while still retaining a relatively high electron mobility [14, 19–21]. This high electron mobility in an amorphous structure is attributed to the symmetric 5s In^{3+} orbitals that dominate the conduction band minimum, thereby reducing cationic disorder [22–25]. The n-type doping in a-IGZO is generally attributed to a large concentration of oxygen vacancy donors. Depending on the local environment, these oxygen-vacancy defect states can appear both deep and shallow within this wide-bandgap material [26–30]. While energetically deep defect states may be related to light-induced instabilities such as positive and negative bias illumination stressing (PBIS/NBIS) [31, 32], they are more commonly associated with persistent trapping effects rather than directly impacting TFT transport properties. In contrast, shallow defect states, located energetically just below the conduction band mobility edge, are expected to act as electron traps that, together with conduction band tail traps, are thought to degrade TFT transport properties [33–36].

To provide a first-principles approach toward optimizing AOS TFTs, one of the first challenges is to resolve the shallow defect-trap density directly on-chip [28, 37]. Ultrabroadband Photoconduction Density of States microscopy (UP-DoS) is an emerging method that provides over 6 orders of magnitude sensitivity by tunable laser excitation of subgap traps directly on the TFT active channel [11, 28, 38]. Previously, UP-DoS could not optically access the shallow defects most directly impacting TFT performance. By adding a tunable difference-frequency generation (DFG) laser, this work resolves this challenge by now ionizing shallow defects to within ~0.1 eV of the conduction-band mobility edge.

A second challenge in AOS TFT optimization lies in establishing a concrete relationship between these shallow defect states and electrical performance [39]. Using UP-DoS to directly measure shallow defects of the active TFT channel, the experimental DoS is fed into a simulation using first-principles Fermi–Dirac statistics to model the resulting electron trapping. This new analytical approach using the TFT experimental subgap DoS may provide the missing link needed to accurately predict key TFT performance metrics directly from processing conditions. As a first step, comparing similar TFTs processed differently demonstrates that the observed changes in shallow defects can reproduce the subthreshold transfer characteristics without adjustable parameters. Then, by introducing a single adjustable parameter, the conduction band Urbach energy, the full TFT transfer curve is simulated directly from the experimental DoS of each TFT. Moreover, we show how these simulations can ultimately be inverted to instead retrieve the total shallow trap density directly from the TFT transfer curve. Lastly, by varying the indium concentration in experimental TFTs, UP-DoS suggests reasonable assignments for all a-IGZO subgap oxygen-vacancy peaks, with each peak identity corroborated by DFT+U defect simulations.

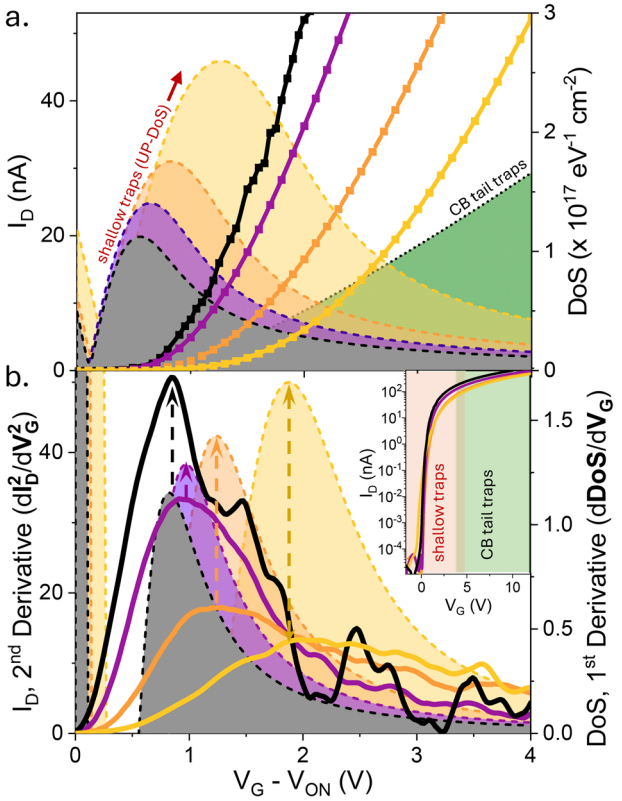


FIGURE 1 | (a) Transfer curves (solid lines) for four a-IGZO TFTs with different processing conditions. Overlaid is the independently measured shallow trap density of states (filled dashed) for each TFT. (b) Corresponding second derivative of the transfer curve (solid lines) overlaid with the first derivative of the experimental density of states (filled dashed) showing peak alignment (dashed arrows). In each TFT, the point of largest curvature in the transfer curve corresponds to when the subgap DoS is changing most rapidly. (*inset*) Zoom-out of transfer curves with the different operating regions shaded.

2 | Results and Discussion

Figure 1a shows four transfer curves (solid lines) plotted on a linear scale as a function of gate overvoltage (I_D - (V_G - V_{ON})). Here, V_{ON} represents the onset of channel conduction and is defined as the lowest applied gate voltage at which the measured drain current is clearly distinguishable from the off-state current. These four curves correspond to four a-IGZO TFTs fabricated under different growth and processing conditions, as summarized by Table S3. Overlaid is the shallow trap density of states (filled dashed) for each TFT that is independently obtained using ultrabroadband photoconduction density of states (UP-DoS) microscopy that uses tunable mid-IR lasers to directly observe the filled shallow defect states. Figure 1b is a corresponding plot of the second derivative of the transfer curves ($\frac{d^2I}{d^2V_G}$) and the first derivative of the density of states (dDoS/dV_G). The inset shows the four transfer curves on logarithmic (I_D - V_G) scales.

Figure 1b shows a striking correlation between each second-derivative curve and the derivative of the shallow trap density of states; namely, both curves peak at the same overvoltage. Specifically, this shows the curvature of the transfer curve is maximal when the shallow trap density of states changes most

16163028, 0, Downloaded from https://advanced.onlinelibrary.wiley.com/doi/10.1002/adfm.78029 by Matt Graham - Oregon State University , Wiley Online Library on [02/09/2026]. See the Terms and Conditions (https://onlinelibrary.wiley.com/terms-and-conditions) on Wiley Online Library for rules of use; OA articles are governed by the applicable Creative Commons License

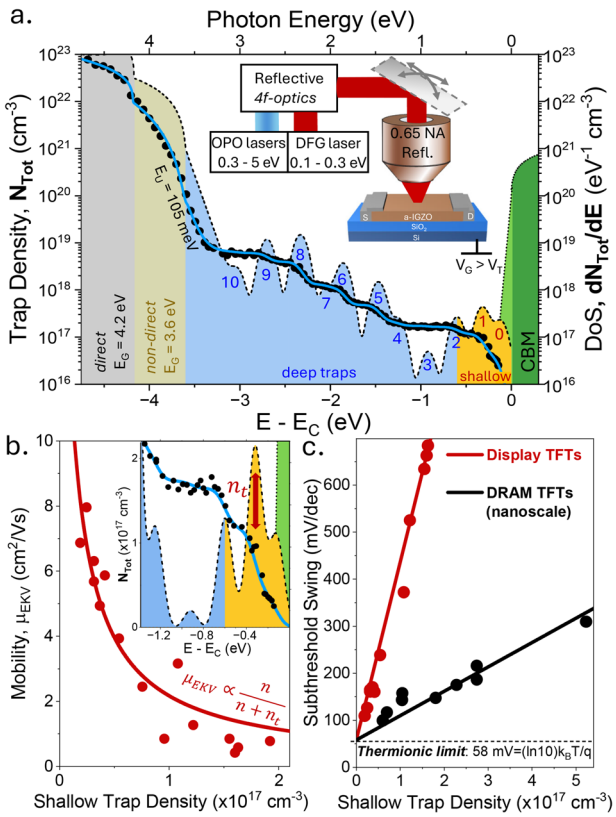


FIGURE 2 | (a) The ultrabroadband photoconduction spectrum (black dots) and the corresponding DoS (first derivative, dashed line) for a representative a-IGZO TFT is characterized by three distinct regions: (i) direct bandgap (gray), (ii) non-direct bandgap (gold), (iii) subgap defects (blue and yellow) composed of Gaussian peaks numbered 0–10 and an Urbach tail. *(inset)* Diagram of the UP-DoS experimental approach. (b) Mobility, μ_{EKV}, as a function of experimentally measured shallow trap density (see inset) for 15 different a-IGZO TFTs. (c) Subthreshold swing plotted against the experimentally measured shallow trap density for TFTs designed for both display (red) and DRAM (black) applications.

rapidly. The best-performing TFT (black) peaks at an overvoltage of ~1 V while the worst-performing TFT peaks at ~ 2 V. This peak shift indicates that the poorer TFT performance is a result of more electron trapping, which persists over a larger overvoltage. Additionally, TFT performance correlates with shallow trap density, as witnessed by the much larger magnitude of the yellow curve compared to the black curve of Figure 1b. The transition between subthreshold and linear behavior occurs approximately when the conduction band tail state density exceeds the shallow trap density, which occurs at an overvoltage of ~1.5 V (~ 2.5 V) for the black (yellow) curve.

Although a-IGZO TFT performance depends primarily on the most shallow traps and conduction band tail state densities, a wealth of information on the subgap trap density is available from UP-DoS analysis, as indicated in Figure 2a. In addition to the shallow traps shown in yellow and labeled as Peak 0 and 1, nine other Gaussian-shaped deep traps (blue) are typically observed in a-IGZO. Furthermore, for the representative a-IGZO TFT shown in Figure 2a, a direct bandgap of 4.2 eV, an optical (non-direct) bandgap of 3.6 eV, and a valence band Urbach energy of 105 meV are extracted and labeled. Depending on processing conditions, optical bandgaps of a-IGZO are typically measured by UP-DoS to be in between 3.0 and 3.6 eV (see Figure S2). As shaded yellow in the inset of Figure 2b, the two most shallow traps and a portion of the third most shallow trap are those responsible for establishing TFT mobility and switching performance. This is shown by the data of Figure 2b in which the EKV mobility is found to degrade dramatically with increasing shallow trap density in a-IGZO display TFTs. This degradation follows the inverse dependence predicted by the trap-limited mobility model (see Equation (2)), [34, 40] with the red solid line showing the best fit to this model. Figure 2c presents the trend in subthreshold slope as shallow trap density increases for display TFTs (red) and nanoscale DRAM TFTs (black). For both TFT device architectures, the relationship between subthreshold swing and trap density is in excellent agreement with a linear fit constrained by the thermionic limit, $\ln(10)k_BT/q$. For details regarding the construction of Figure 2b,c, the mobility correlations in nanoscale DRAM TFTs, and the correlations between shallow trap density and negative-bias temperature stress (NBTS), see Section S5 and Figures S8 and S14.

Figure 3 presents a subset of transfer curves and UP-DoS data of the DRAM TFTs used to construct Figure 2c. The I_D-(V_G - V_{ON}) transfer curves included in Figure 3a are of dramatically different quality. Figure 3b demonstrates that a-IGZO TFT performance depends strongly on trap density (upper panel) and corresponding subgap DoS (lower panel). The best-performing (blue) TFT transfer curve has a much smaller trap density than that of the worst (black) TFT. It turns out that defect states only within ~0.65 eV of the conduction band mobility edge directly act as electron traps and serve to degrade a-IGZO switching and mobility performance, as is suggested from the comparatively well-performing red curve despite its large deep trap density. As the shallow trap density increases in Figure 3b, a larger gate voltage is required to fill these traps and to modulate the quasi-Fermi level out of the subthreshold into the linear regime of TFT operation. This larger shallow trap density increases the subthreshold slope and the value of the threshold voltage relative to the turn-on voltage (V_T - V_{ON}), and correspondingly decreases the total drift mobility of the TFT. Here, V_{ON} is defined as the onset of channel conduction, while V_T is the threshold voltage extracted from the transfer curve using the linear extrapolation method. Consequently, the value of V_T - V_{ON} serves as a proxy for the Gaussian-shaped shallow electron trap density, since it is proportional to the number of traps that must be filled between turn-on and the transistor reaching the linear gate-voltage operating regime.

As shown in the lower panel of Figure 3b, three main Gaussian-shaped traps are experimentally observed in this energy range. Only the two traps closest to the conduction band mobility edge (red shading) are relevant to a-IGZO TFT electrical operation. DFT+U assessment (see Section 2.2) assigns all three peaks to oxygen vacancy donors. Moreover, peaks 1 and 2 are ascribed to a Ga-rich, 3-atom and an In-rich, 4-atom cation coordination around a missing oxygen, respectively, as sketched in Figure 3b.

16163028, 0, Downloaded from https://advanced.onlinelibrary.wiley.com/doi/10.1002/adfm.78029 by Matt Graham - Oregon State University , Wiley Online Library on [02/09/2026]. See the Terms and Conditions (https://onlinelibrary.wiley.com/terms-and-conditions) on Wiley Online Library for rules of use; OA articles are governed by the applicable Creative Commons License

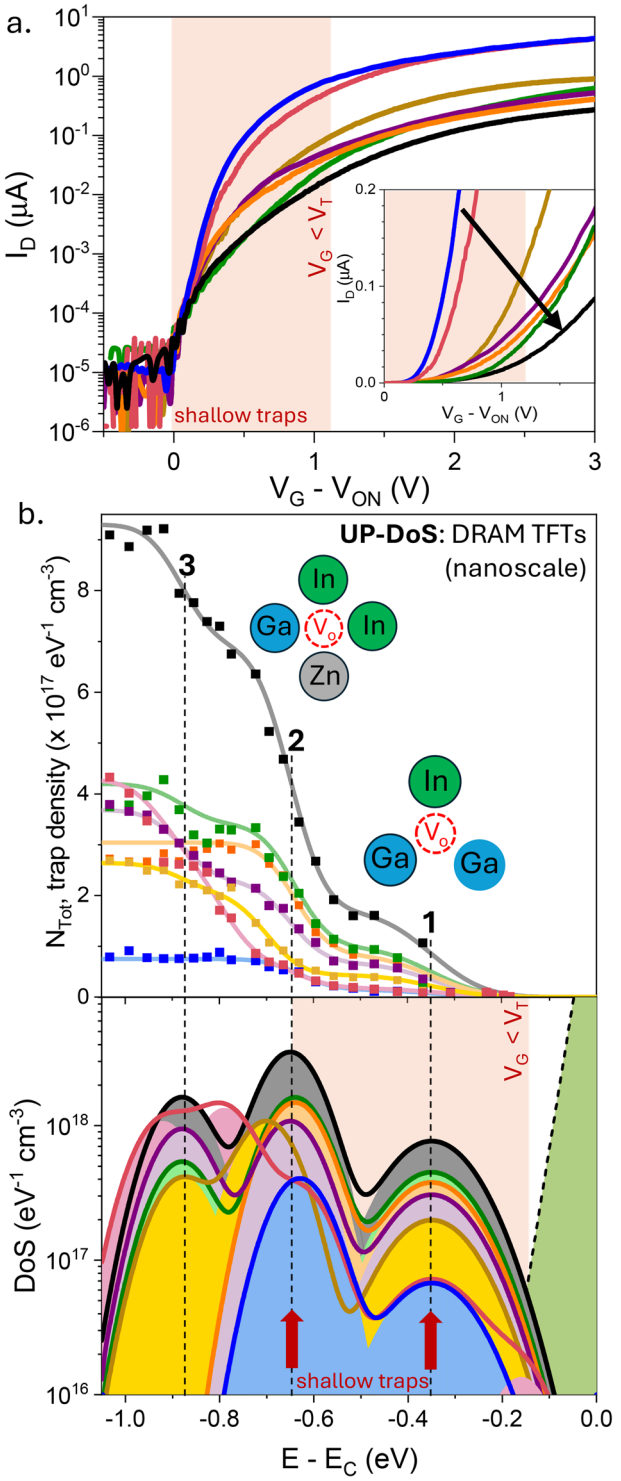


FIGURE 3 | (a) Transfer curves (V_{DS} = 1 V) of 7 different nanoscale DRAM a-IGZO TFTs processed under different growth and annealing conditions. (b) The ultrabroadband photoconduction DoS spectra near the conduction band mobility edge for the 7 corresponding TFTs show a stepwise decreasing trap density. **(lower panel)** The resulting experimentally measured subgap density of states for each TFT. The shallow trap density, highlighted by the red-shaded region, is directly correlated with TFT performance.

2.1 | Simulation of Transfer Curves from Experimental DoS

Figure 4a plots the experimentally measured subgap DoS (filled dashed), and the corresponding simulated mobility when the quasi-Fermi level energy, F_n, is modulated from -0.64 to 0.2 eV (red line, right *y*-axis) relative to the conduction band mobility edge. As the defect states originate from the underlying atomic structure and local coordination environment of the semiconductor, their energetic distribution is taken to be constant as a function of F_n, with only the occupation probability of the states varying. Using the full DoS model shown in Figure 4a, the trapped electron density, $n_T(F_n) = Q_T(F_n)/q$, and free electron density, $n(F_n) = Q(F_n)/q$, are calculated using Fermi–Dirac statistics (see Section 4.3 for details). From $Q_T(F_n)/q$ and $Q(F_n)/q$, the simulated TFT drift mobility, $\mu_{SIM}(F_n)$, is subsequently obtained from Equation (2). When the quasi-Fermi energy is positioned 0.64 eV below the conduction band mobility edge (horizontal dotted line), essentially all electrons induced by gate overvoltage are trapped, resulting in a very small drift electron mobility. Conversely, for $V_G = 10$ V, the quasi-Fermi level energy is simulated to be within ~ 80 meV of the conduction band mobility edge, yielding a corresponding drift mobility of ~10 cm^2 V^{-1} s^{-1}.

To better visualize electron trapping in a-IGZO TFTs, Figure 4b plots the experimentally measured subgap DoS (filled dashed, right *y*-axis) on a gate voltage axis in order to directly compare the relevant trap distribution to the experimental TFT transfer curve (solid line, left *y*-axis). More specifically, the dashed line represents the subgap DoS at the given quasi-Fermi level energy, which is directly mapped to a gate voltage axis using the charge sheet approximation model (see Section 4.3). At the smallest gate overvoltages, Figure 4b shows that the oxygen vacancy states (V_O), peaks 1 and 2, dominate the subgap DoS, such that most electrons induced into the channel are trapped by these states. As the gate voltage increases, the quasi-Fermi level moves toward the conduction band, filling more V_O trap states. This quasi-Fermi level modulation results in an exponentially increasing fraction of electrons populating extended states as free carriers. The larger the shallow V_O trap density, the more sluggish the exponential turn on, as observed by Figure 2c. When the quasi-Fermi level is modulated into the subgap DoS region that is dominated by conduction band tail states, most shallow V_O trap states become filled, causing the TFT to transition out of subthreshold and enter the linear operating regime ($V_G > V_T$).

Applying the DoS model outlined in Figure 4a, Figure 4c presents a simulation of the trapped electron density ($n_T(V_G) = Q_T(V_G)/q$, red line), and the free electron density ($n(V_G) = Q(V_G)/q$, yellow line) induced into the channel by the applied gate overvoltage. The simulated trends agree well with the experimentally extracted gate voltage-induced electron densities (black and brown lines) obtained from the TFT transfer curve. In the subthreshold region, as a consequence of the Gaussian shallow V_O trap peaks, $Q_T(V_G)/q$ increases linearly with gate voltage and $Q(V_G)/q$ increases exponentially. Above threshold ($V_G > V_T$), Figure 4c reveals that both Q_T/q and Q/q increase

16163028, 0, Downloaded from https://advanced.onlinelibrary.wiley.com/doi/10.1002/adfm.78029 by Matt Graham - Oregon State University , Wiley Online Library on [02/09/2026]. See the Terms and Conditions (https://onlinelibrary.wiley.com/terms-and-conditions) on Wiley Online Library for rules of use; OA articles are governed by the applicable Creative Commons License

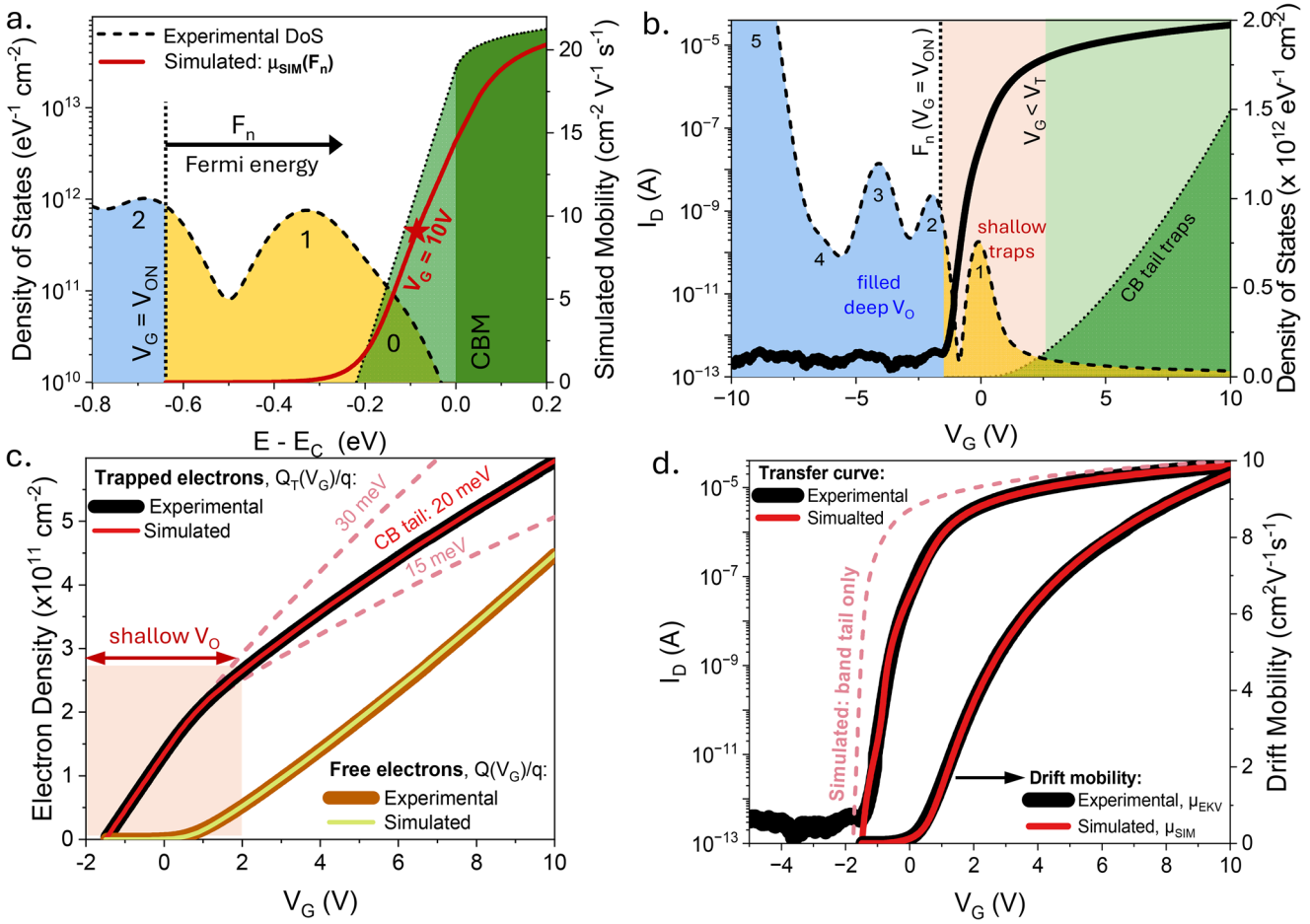


FIGURE 4 | (a) TFT simulated mobility (μ_{SIM}, red line) as a function of quasi-Fermi level energy. μ_{SIM} is obtained by modeling trapping in experimentally measured Gaussian-like subgap states (filled dashed) and conduction band tail states (filled green). (b) a-IGZO TFT transfer curve (black, left *y*-axis) plotted with the experimentally measured subgap defect DoS (filled dashed, right *y*-axis) converted to a gate voltage axis, showing the dominant electron traps for different TFT operating regions. (c) Experimentally extracted (thick lines) and DoS simulated (thin lines) free and trapped electron density as a function of gate voltage. (d) DoS simulated transfer and mobility curves (red) plotted with experimentally measured data (black). The red dashed line is the simulated transfer curve if all Gaussian trap contributions are excluded (i.e., only tail states).

linearly. The change of dominant active trap, from Gaussian-shaped V_O (subthreshold) to the exponential conduction band tail (above threshold), is evident by the change of slope in $Q_T(V_G)/q$, which occurs at $V_G \approx V_T$. In the subthreshold operating regime, since virtually all states induced into the channel by applied gate voltage are trapped in Gaussian-shaped V_O, the slope of $Q_T(V_G)/q$ is simply C_{ox}/q. Above this threshold, the slope of the line is C_{ox}/q multiplied by the fraction of carriers trapped in the exponential band tail state, which depends on the exponential slope parameter, W_{TA}. To fit the experimental data, a conduction-band tail Urbach energy $W_{TA} = 20$ meV is required. We consider this value to be a reliable estimate of the conduction band tail Urbach energy and a reflection of the amount of disorder on the cationic sub-lattice for this a-IGZO TFT. However, it is important to note that while shallow V_O traps dominate the subthreshold region, significant above-threshold non-idealities, such as series resistance or fringe current effects [41], may affect W_{TA} estimation by this method. Both series resistance and fringe current artifacts are minimized in this example by choosing a large-area TFT with a large W/L ratio (W = 200 μm, L = 10 μm).

To complete this simulation using experimental DoS, the simulated gate voltage induced electron densities, $Q_T(V_G)/q$ and $Q(V_G)/q$, are employed to determine the corresponding TFT drift mobility, $\mu_{SIM}(V_G)$, and drain current, $I_{D,SIM}(V_G)$. Figure 4d shows remarkable agreement between the final simulated (red line) and the overlaid experimental transfer curve. Likewise, the simulated drift mobility curve (red line, right *y*-axis) shows excellent agreement with the overlaid experimental mobility curve. The red-dashed line plots a simulated transfer curve if the conduction band tail is the only source of trapping, showing idealized behavior of an a-IGZO TFT without shallow V_O traps. Collectively, the above method accurately simulates the transfer curve directly from experimentally measured subgap DoS, and demonstrates that both conduction band tail and shallow Gaussian trap states are required in order to simulate transfer curve behavior in an a-IGZO TFT.

Presented in Figure 5 are simulated gate voltage-dependent (a) trap density, (b) mobility, and (c) transfer curves for varying conduction band Urbach energies of 10 to 30 meV. In these

16163028, 0, Downloaded from https://advanced.onlinelibrary.wiley.com/doi/10.1002/adfm.78029 by Matt Graham - Oregon State University , Wiley Online Library on [02/09/2026]. See the Terms and Conditions (https://onlinelibrary.wiley.com/terms-and-conditions) on Wiley Online Library for rules of use; OA articles are governed by the applicable Creative Commons License

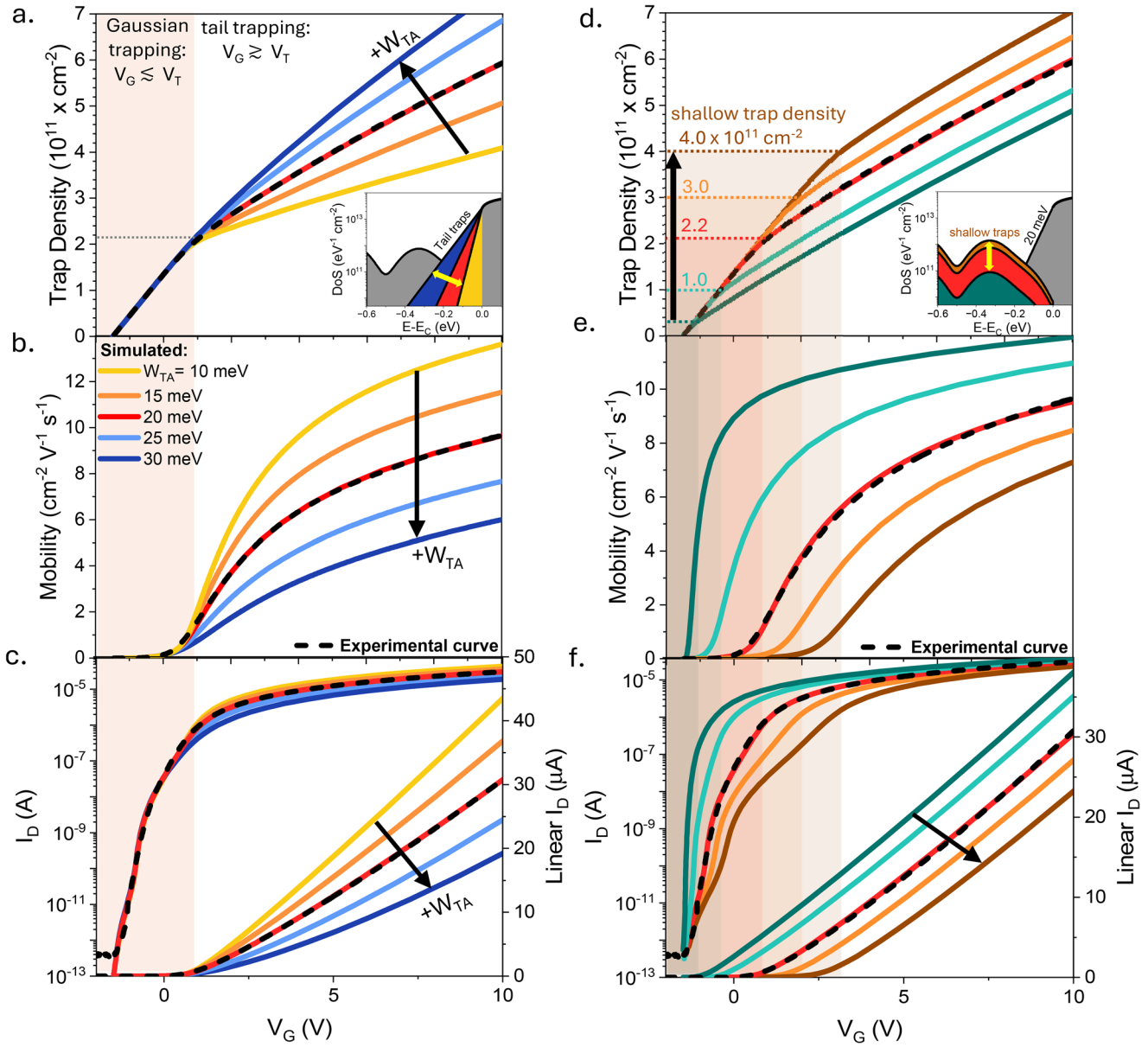


FIGURE 5 | DoS is used to simulate (a) TFT gate voltage induced trap density, (b) mobility, and (c) transfer curve as a function of gate voltage for different conduction band tail state Urbach energies. The slope of the transfer curve in the linear regime decreases with increasing Urbach energy, while the subthreshold behavior is unaffected. DoS simulated (d) TFT gate voltage induced trap density, (e) mobility, and (f) transfer curve for different shallow V_O trap densities. With increasing shallow V_O trap density, the threshold voltage and subthreshold swing increase because more trap states must be filled before the TFT enters the linear regime.

simulations, V_{ON} is set to -1.5 V to match the experimental TFT curve (black dashed). While subthreshold region behavior (shaded in red) largely remains constant, enhanced trapping at large gate voltages occurs with increasing Urbach energy (Figure 5a), resulting in reduced mobility and a corresponding reduced current (Figure 5b,c). Above the threshold voltage, the simulated value of W_{TA} is directly related to the slope of both $Q_T(V_G)/q$ and the corresponding transfer curve. This implies that for an idealized TFT, the only two parameters that increase the common performance metricof TFT field-effect mobility (μ_{FE}), which is the incremental mobility in the linear operating regime, are the conduction band tail Urbach Energy W_{TA} and the trap-free mobility μ_o.

In Figure 5, the simulated (d) trap density, (e) mobility and (f) transfer curve are plotted when varying the total shallow V_O trap density, from 4 to 0.25 × 10^{11} cm^{-2}. The colored shaded region marks the subthreshold region for each simulated V_O shallow trap density. The threshold voltage increases with trap density because more traps are occupied before the TFT enters the linear regime. In Figure 5d, the first linear section of the gate-induced trap density (subthreshold) extends with increasing V_O shallow traps, while the second linear section (above threshold) exhibits a corresponding linear offset. Notably, the slope of both linear sections remains constant across all shallow trap densities. Comparing Figure 5a,d, it is evident that the induced trap density as a function of gate voltage is characterized by two linear

16163028, 0, Downloaded from https://advanced.onlinelibrary.wiley.com/doi/10.1002/adfm.78029 by Matt Graham - Oregon State University , Wiley Online Library on [02/09/2026]. See the Terms and Conditions (https://onlinelibrary.wiley.com/terms-and-conditions) on Wiley Online Library for rules of use; OA articles are governed by the applicable Creative Commons License

functions. The first linear function involves shallow V_O trapping in the subthreshold regime, where the amount of traps controls the extension of the line along the gate voltage axis. The second line, corresponding to the above threshold regime, is due to the conduction-band tail trapping, where the slope is controlled by the Urbach energy and the offset by the shallow V_O trap density. Consequently, as indicated by the dotted lines in Figure 5d, for each $Q_T(V_G)/q$ curve, the shallow V_O trap density is effectively equal to the gate voltage-induced trap density at the point of slope change. Remarkably, since $Q_T(V_G)/q$ curves can be directly obtained from experimental transfer curves (see Section 4.3), the total shallow V_O trap density in a TFT can be simply estimated without requiring the use of a defect characterization technique, such as UP-DoS. The conduction band tail Urbach energy can likewise be estimated from the slope of the second linear segment of the $Q_T(V_G)/q$ curve. However, in contrast to V_O shallow-trap estimation, the accuracy of Urbach Energy estimation depends on precise knowledge of μ_0 and on minimizing series resistance and peripheral current artifacts.

In Figure 5e the TFT drift mobility decreases and the threshold voltage increases with increasing shallow V_O trap density as more electrons are being trapped. These mobility curves are stretched and increasingly distorted along the gate-voltage axis as shallow trap density increases. The corresponding transfer curves, as shown in 5f, are also stretched and distorted along the gate-voltage axis. Figure 5f shows the evolution of a kink in the transfer curve, originating from enhanced trapping and sluggish modulation of the Quasi-Fermi level. Comparing Figure 5c to Figure 5f suggests that this distortion (or kink) observed in the simulated transfer curve is a result of a high V_O shallow trap density. Finally, it is important to note that the transfer curves can only be accurately simulated when the specific peak energies and widths measured by UP-DoS are used. For examples of how the transfer curve is expected to be modulated by a different Gaussian peak energy and width, see Figure S9.

The upper panel of Figure 6a shows a plot of the shallow trap density and trap density across the full band gap (inset) for 5 different a-IGZO TFTs developed for display panel applications. The bottom panel of Figure 6a plots the corresponding subgap DoS, revealing one shallow oxygen vacancy defect peak. Figure 6b presents the comparison between experimentally measured transfer curves (solid lines) and DoS simulated transfer curves (dashed lines). The red dashed line simulates an idealized TFT without shallow oxygen vacancy traps. Black (and gray) dashed lines are simulated transfer curves by using the shallow oxygen vacancy DoS experimentally measured in each TFT and show excellent agreement with each corresponding experimental curve.

Remarkably, the only adjustable simulation parameter in the Figure 6b simulated transfer curves is the conduction band tail Urbach energy, $W_{TA} = 23$ –31 meV, which is associated with the degree of cationic disorder within the amorphous oxide semiconductor and primarily modulates the slope of the linear operating regime. Figure 6b shows that robust agreement is achieved between experiment and simulation only when both shallow trap filling (subthreshold, from UP-DoS) and conduction band tail trap filling (above threshold) are included. The simulated transfer curves with no adjustable parameters (i.e., assuming a fixed W_{TA} across all TFT processing conditions) also agree well with the experimental curves until the transition to the linear operating regime (see Figure S10). As such, the specific curvature of the subthreshold region, as well as characteristics such as subthreshold swing and the threshold voltage relative to turn-on voltage (V_T - V_{ON}), which in turn also pinpoint the onset of the linear operating regime, are well simulated from the experimentally measured subgap DoS. The simulated conduction band tail Urbach energy, along with the measured shallow trap density and electrical characteristics for each TFT, are summarized in Table 1, with the specific processing conditions additionally listed in Table S3.

Figure 6c upper panel plots the extracted (solid lines) and DoS simulated (dashed lines) trap densities, $Q_T(V_G)/q$, as a function of gate voltage for the 5 different TFTs. By including the measured experimental shallow V_O density in each TFT simulation, an excellent agreement between experimental and simulated results is evident. In accordance with Figure 5d, the shallow oxygen vacancy trap density can be extracted from the total trap density value at the point of slope change in $Q_T(V_G)/q$ curve for each TFT. Precisely, this point of slope change occurs at the gate voltage where the 2nd derivative of the transfer curve peaks (see Figure 1b). Alternatively, the shallow oxygen vacancy trap density can be approximated by the total trap density taken at $V_G \approx V_T$. Note that, in the idealized DoS simulation (red dashed), no point of slope change occurs as the shallow trap density is zero, and likewise, $V_T = 0$, so that the total trap density evaluated at $V_G \approx V_T$ is correspondingly zero. For large gate voltages, the extracted trap densities of the different TFTs diverge from each other owing to differences in thier respective W_{TA} values, which augments the corresponding transfer curves' slope in the linear operating regime. Figure 6c lower panel plots simulated (dashed lines) and measured mobility (solid line) curves for each TFT. In agreement with simulated trends in Figure 5e, the experimentally observed increase in shallow oxygen vacancy trap density results in a reduction in TFT drift mobility and an associated increase in the threshold voltage relative to turn-on voltage, V_T - V_{ON}. Lastly, it is important to mention that while our method of correlating experimentally measured UP-DoS with measured electrical performance is highly predictive for the 25 different a-IGZO TFT configurations studied, extreme conditions (e.g., an unusual abundance of hydrogen, peroxides, or large device non-idealities) can exist that will make this analytical approach prohibitive.

2.2 | Experimental DoS Peak Correspondence with DFT+U Assignments

The objective of the remaining two sections is to identify the microscopic origin of the experimentally observed subgap defect states in the TFTs investigated in this work. The rationale for excluding secondary defects such as hydrogen and metal vacancies, is presented in Figures S15, S16, and S17. Figure 7a presents the DFT+U simulated DoS for a pristine (no oxygen vacancies) a-IGZO unit cell (black) and for cells possessing oxygen vacancies with ZnZnZnIn (gray), GaGaGaIn (blue) and InInInGa (green) nearest-neighbor coordination environments. The valence band maximum defines the reference energy (VBM = 0 eV). The Fermi level energy (dotted lines) and conduction band minimum (solid

16163028, 0, Downloaded from https://advanced.onlinelibrary.wiley.com/doi/10.1002/adfm.78029 by Matt Graham - Oregon State University , Wiley Online Library on [02/09/2026]. See the Terms and Conditions (https://onlinelibrary.wiley.com/terms-and-conditions) on Wiley Online Library for rules of use; OA articles are governed by the applicable Creative Commons License

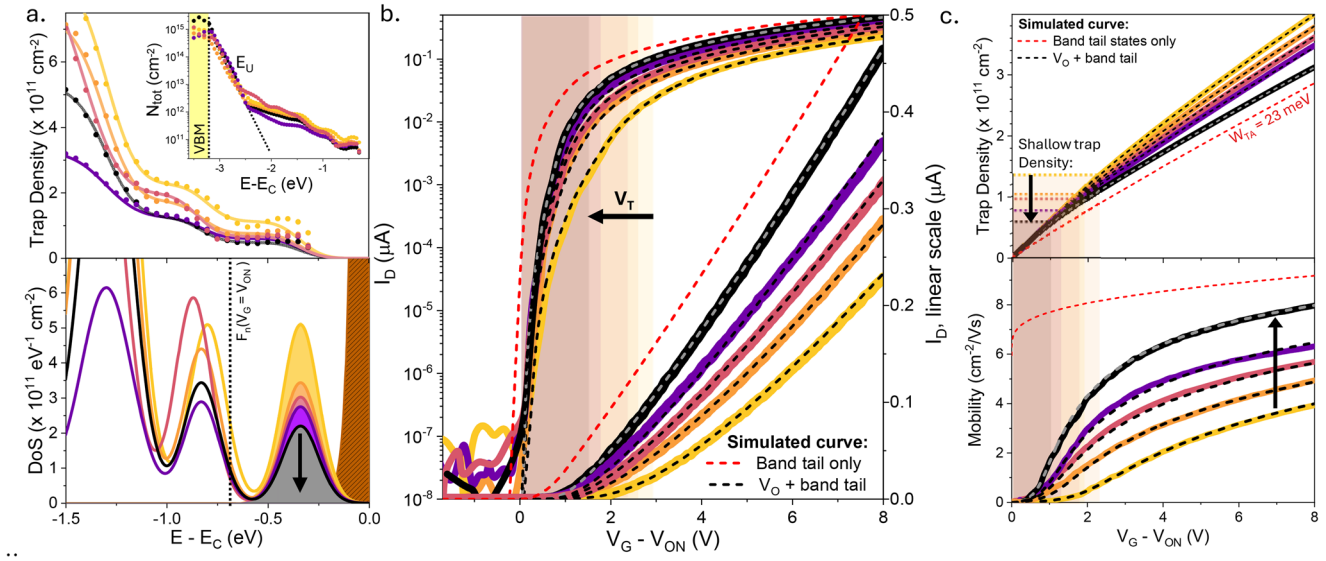


FIGURE 6 | (a) Measured shallow trap density (upper panel) for 5 a-IGZO TFTs with different processing conditions and (lower panel) corresponding subgap DoS revealing one shallow oxygen vacancy defect peak. Inset displays the full UP-DoS trap density. (b) Experimental TFT transfer curves (V_{DS} = 1 V, solid lines) compared to simulated transfer curves (dashed lines) generated using measured shallow subgap DoS. (c) Experimental (solid lines) and DoS simulated (dashed lines) gate voltage induced trap density (upper panel) and drift mobility (lower panel).

TABLE 1 | Experimentally measured shallow V_O peak trap density for five a-IGZO TFTs with different processing conditions compared to the corresponding electrical characteristics and simulated conduction band tail Urbach energy.

Line color	V_O Peak density $\times 10^{11}$ [$cm^{-2}eV^{-1}$]	S.S [mV/dec]	Mobility, μ_{EKV} [$cm^2 V^{-1} s^{-1}$]	Simulated W_{TA} [meV]
Black	2.2	126	8.0	23
Purple	2.8	165	6.3	26
Red	3	161	5.7	28
Orange	3.5	170	4.9	30
Yellow	5.1	238	3.9	31

lines) are marked in each simulation. The specific oxygen vacancy coordination environments shown in Figure 7a are selected as an example from a total of 160 simulated vacancy configurations (80 per unit-cell structure). For all simulated cells, including the pristine cell, localized states appear near the valence band maximum and are attributed to the bond length disorder on the anion (oxygen) sublattice. For the pristine case, the Fermi level energy is positioned just above these localized donor-like states.

In contrast, for all cells containing an oxygen vacancy, the Fermi level is shifted toward the conduction band and is positioned above a new defect state created within the bandgap. This new oxygen vacancy defect state appears deep for the Zn-rich oxygen vacancy cell, near the midgap for the Ga-rich oxygen vacancy cell, and shallow for the In-rich oxygen vacancy-metal coordination environment. The subgap oxygen vacancy defect state appears in all DFT+U simulations in which the neighboring cation coordination relaxes inward toward the vacancy. When neighboring coordinated cations relax outward from the vacancy, the associated defect peak appears within the conduction band, with its corresponding Fermi level positioned above the conduction band minimum (see Section S3). For all simulations featuring a subgap oxygen vacancy state, the DFT+U calculated conduction band minimum is shifted to higher energies, increasing the bandgap relative to that of the pristine (oxygen defect-free) cell. This is in contrast to the case of an oxygen vacancy defect state appearing above the conduction band minimum, in which the approximate bandgap of the pristine cell is retained.

Since an oxygen atom is removed at random in all simulations, it is reasonable to sum over each calculated DoS for one cell structure to observe statistical trends. Figure 7b (upper panel) plots the total simulated DFT+U DoS as summed over all 80 simulations (black line) and for all subgap oxygen vacancies (red line). Additionally, all oxygen vacancies with no sole dominant metal coordination (1:1:1 triple and 2:2 quadruple vacancy-cation coordination, e.g., In–Ga–Zn or In–In–Zn–Zn) are plotted in filled beige. When all simulations are summed together, the defect states positioned near the valence band, ascribed to anion sublattice bond length disorder, give rise to a pronounced smearing of the valence band. This valence band smearing is experimentally observed as an exponential Urbach tail in the valence band (W_{TD} ≈ 100 meV) and as the emergence of an optical (non-direct) bandgap in the material (E_g ≈ 3.0–3.6 eV) [42–45].

16163028, 0, Downloaded from https://advanced.onlinelibrary.wiley.com/doi/10.1002/adfm.78029 by Matt Graham - Oregon State University , Wiley Online Library on [02/09/2026]. See the Terms and Conditions (https://onlinelibrary.wiley.com/terms-and-conditions) on Wiley Online Library for rules of use; OA articles are governed by the applicable Creative Commons License

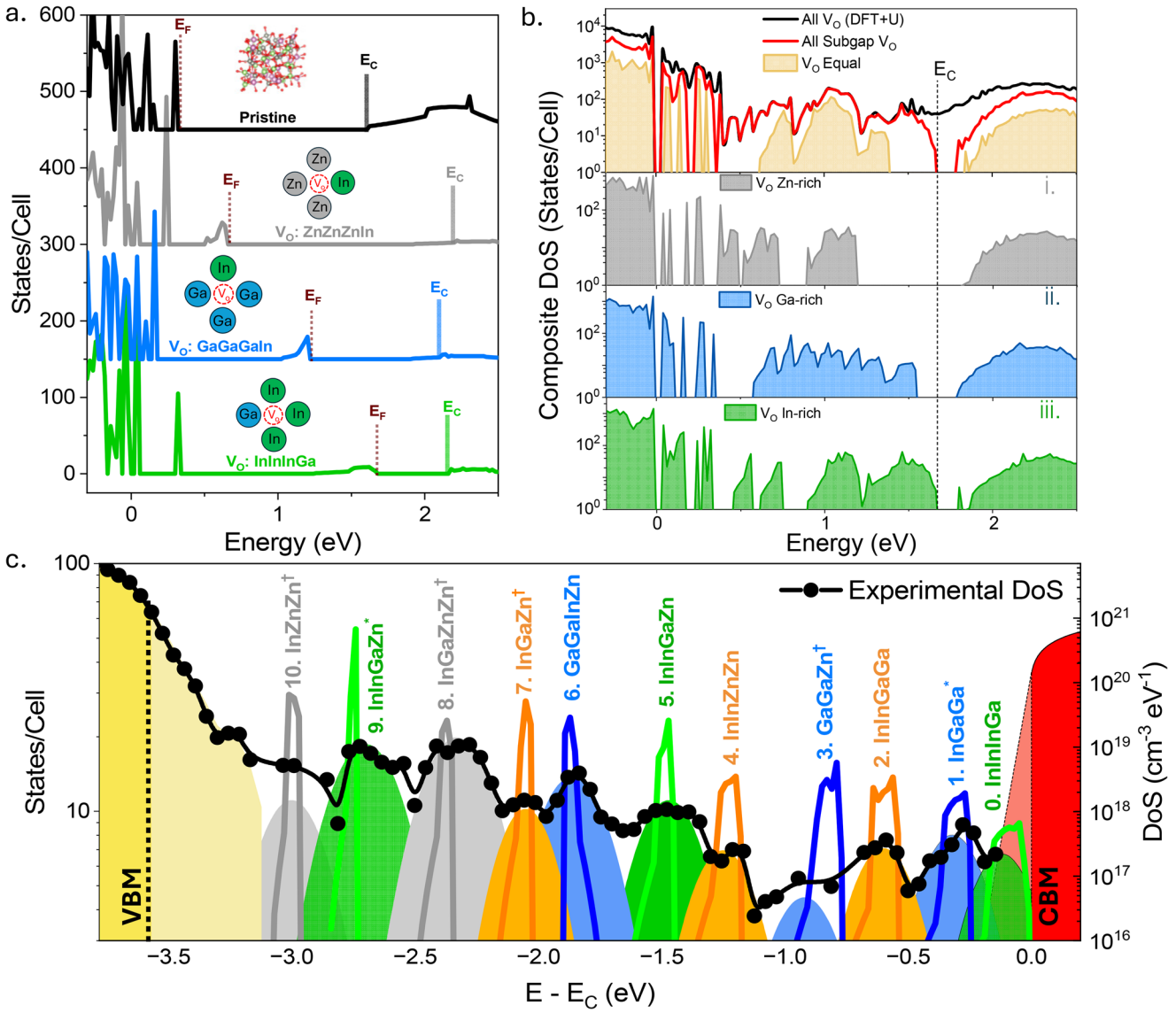


FIGURE 7 | (a) Representative of DFT+U–calculated density of states (DoS) for a pristine unit cell (black line) and for cells with Zn-Zn–Zn–In (gray line), Ga–Ga–Ga–In (blue line), and In–In–In–Ga (green line) metal coordinated oxygen vacancies (V_O). (b) DFT+U calculated total summation of DoS for different oxygen vacancy configurations: all DFT+U (black), all subgap V_O (red), equal V_O cation coordination (beige), Zn-rich V_O (gray), Ga-rich V_O (blue), and In-rich V_O (green). (c) Experimentally measured subgap DoS for a-IGZO (black dots), together with representative DFT+U-calculated oxygen vacancy defect states attributed to the experimental defect peaks (colored lines).

Figure 7b (lower panels) plots DoS by summing over cells with oxygen vacancies in Zn- (gray), Ga- (blue), or In- (green) dominated coordination environments. Oxygen vacancy sites with Zn-rich metal coordination environments exclusively appear in the lower portion of the bandgap. Consequently, Zn-rich oxygen vacancies are unlikely to affect TFT performance metrics such as subthreshold swing or drift mobility. On the other hand, Ga-rich and In-rich oxygen vacancy coordination environments often create shallow electron trap states that can degrade a-IGZO TFT performance.

Figure 7c compares experimentally measured DoS with selected oxygen-vacancy defect states calculated using DFT+U. Black dots correspond to the direct numerical differentiation of the raw, experimentally obtained trap density spectrum, with no smoothing. The colored Gaussian peaks represent the DoS for each measured defect peak, obtained from error-function fitting to the same spectrum. Colored lines represent DFT+U calculated oxygen vacancy peaks for a specific cation coordination environment. Many oxygen-vacancy defect peaks with different metal coordination environments overlap in the DoS, allowing multiple possible identifications of the experimental data. The peaks shown in Figure 7c best match the experimentally observed energetic positions and agree with the indium enrichment results discussed in the next section. Experimental peaks 1 and 9 can be reasonably assigned to a single coordination environment, as they have no plausible competing DFT+U peak energy matches and are marked with an asterisk *. For peaks 0, 2, 4, 5, and 6, DFT+U cannot assign them to a unique coordination environment, but the dominant metal in each peak can still be identified. Specifically, experimental peaks 0, 2, 4, and 5 are identified as involving coordination environments in which

16163028, 0, Downloaded from https://advanced.onlinelibrary.wiley.com/doi/10.1002/adfm.78029 by Matt Graham - Oregon State University , Wiley Online Library on [02/09/2026]. See the Terms and Conditions (https://onlinelibrary.wiley.com/terms-and-conditions) on Wiley Online Library for rules of use; OA articles are governed by the applicable Creative Commons License

TABLE 2 | Experimental UP-DoS defect peak energies (CBM = 0) and trap densities for all peaks 0–10. Each peak is matched with dominant oxygen vacancy coordination environments calculated by DFT+U.

Peak #	Energy eV	Density 10^{16}cm^{-3}	Dominant V_O cation coordination
0	0.12	2.0	**InInInGa**, InInZn
1*	0.32	9.7	**InGaGa**
2	0.60	4.8	**InInGaGa**, InInZnZn, InInGaZn,
3†	0.92	0.9	**GaGaZn**, GaGaGaIn, InZnZnZn
4	1.25	4.0	**InInZnZn**, InInGaZn
5	1.47	26	**InInGaZn**, InInGaGa, InInGa,
6	1.86	66	**GaGaInZn**, GaGaZn, GaGaIn
7†	2.05	18	**InGaZn**, GaGaInZn, GaGaIn
8†	2.33	270	**InGaZnZn**, GaGaInZn, GaGaZnZn
9*	2.70	210	**InInGaZn**
10†	3.03	27	**InZnZn**, InGaGa, GaZnZnZn

*Specific V_O coordination environment identified.
†Multiple In-poor cation coordination environments possible.

at least 2 neighboring metals are indium, whereas peak 6 is classified as Ga-rich. Finally, peaks 3, 7, 8, and 10 are marked with a dagger † to indicate multiple DFT+U matches are possible and unambiguous peak identification is not possible. However, Section C will show these peaks are In-poor. Table 2 summarizes the DFT+U peak identification results, while Table S4 provides a complete summary of all calculated defect peaks.

2.3 | a-IGZO Indium Enrichment DoS Trends

The objective of this section is to experimentally identify which oxygen vacancy peaks in these a-IGZO TFTs involve indium-rich cation coordination environments. Indium enrichment is accomplished via co-sputtering from an indium oxide target.

Figure 8a presents transfer curve extracted trap density (volumetric, $Q_t(V_G)/(q \times d)$, d ≈10 nm) versus overvoltage plots for a-IGZO TFTs with different amounts of indium incorporated into the channel. The extracted trap density increases with increasing co-sputtering power and appears to saturate for a co-sputtering power above ∼ 60 W. Thus, in this experiment, a-IGZO quality, in terms of shallow trap density, degrades with increased indium incorporation. This is expected since process optimization of co-sputtered TFTs has not been undertaken. Importantly, the goal of In-enrichment is to aid in oxygen vacancy peak assignment without introducing other interfering effects from process optimization.

In Figure 8b, the UP-DoS trap density and corresponding DoS are compared across the full bandgap for the 0 W (black, no co-sputtering) and 100 W (green, maximum Indium incorporation) a-IGZO TFTs. In the most In-rich TFT, an additional feature near the valence band appears at ∼3.0 eV with an energy and lineshape closely matching the indirect bandgap of a possible In_2O_3 phase [46, 47]. Comparing the total experimental trap density just below this bandgap feature, the total oxygen vacancy trap density (shallow and deep) remains approximately equal between the two samples, while the amplitudes of individual defect peaks vary by ∼2–8× after In-enrichment. In the upper portion of the bandgap (for experimental peak numbers 5, 4, 3, 2, and 0), the trap density of In-rich a-IGZO increases significantly. This observation is in strong agreement with the overlaid DFT+U DoS (light green), which shows a pronounced increase in the DoS of In-rich oxygen-vacancy states in this energy region. In the midgap, experimental peaks numbered 6, 7, and 8 are all observed to decrease with In-growth power, consistent with a Ga- or Zn-rich oxygen vacancy coordination environment. This assignment is further supported by DFT+U simulations, which predict few or no In-rich defect peaks in this region relative to the total. Finally, near the valence band edge, experimental peak 9 increases with indium incorporation, consistent with DFT+U calculations that identify an In–In–Ga–Zn-coordinated oxygen vacancy at the corresponding energy.

From the perspective of TFT electrical performance, the most shallow oxygen vacancy traps are of primary interest. Figure 8c shows the UP-DoS trap density (upper panel) and DoS (lower panel) for this upper portion of the bandgap for co-sputtering powers 0–100 W. In the upper panel, DFT+U-simulated oxygen vacancy peaks with specific cation coordination environments are proposed. Defect peak numbers 0, 2, 4, and 5 increase systematically with In-incorporation and are attributed to In-rich oxygen vacancy coordination environments. Conversely, defect peak numbers 1 and 6 decrease with increasing indium power, suggesting instead a Zn- or Ga-rich oxygen vacancy coordination. This further confirms that shallow peak 1 is a likely GaGaIn 3-atom-coordinated oxygen vacancy. This Ga–Ga–In-coordinated oxygen vacancy is observed to be the dominant trap driving the subthreshold behavior and degradation characteristics of well-functioning a-IGZO TFTs (see Figure 4). To a large extent, process optimization of an In:Ga:Zn = 1:1:1 a-IGZO TFT involves reducing the density of this Ga-rich peak 1 as much as possible. Defect peak number 0 is attributed to an In-rich coordinated oxygen vacancy environment (In–In–In–Ga or In–In–Zn). This peak is generally observed to have a lower defect density in the UP-DoS of 1:1:1 a-IGZO TFTs. However, for optimization toward a well-functioning indium-rich a-IGZO TFT, this defect peak must be suppressed.

3 | Conclusions

The subgap density of states of a-IGZO TFTs are measured using tunable lasers from the valence band to within 0.14 eV of the conduction band mobility edge by ultrabroadband photoconduction density of states (UP-DoS) microscopy. First-principles device-physics simulation using the experimentally obtained defect DoS, together with statistical analysis of 25 TFTs fabricated under varying processing conditions, demonstrates that the density of shallow oxygen vacancies can critically control TFT metrics such as subthreshold swing, threshold voltage, and drift mobility. For a set of TFTs under varying processing conditions, the simulation using UP-DoS data accurately reproduces the subthreshold TFT

16163028, 0, Downloaded from https://advanced.onlinelibrary.wiley.com/doi/10.1002/adfm.78029 by Matt Graham - Oregon State University , Wiley Online Library on [02/09/2026]. See the Terms and Conditions (https://onlinelibrary.wiley.com/terms-and-conditions) on Wiley Online Library for rules of use; OA articles are governed by the applicable Creative Commons License

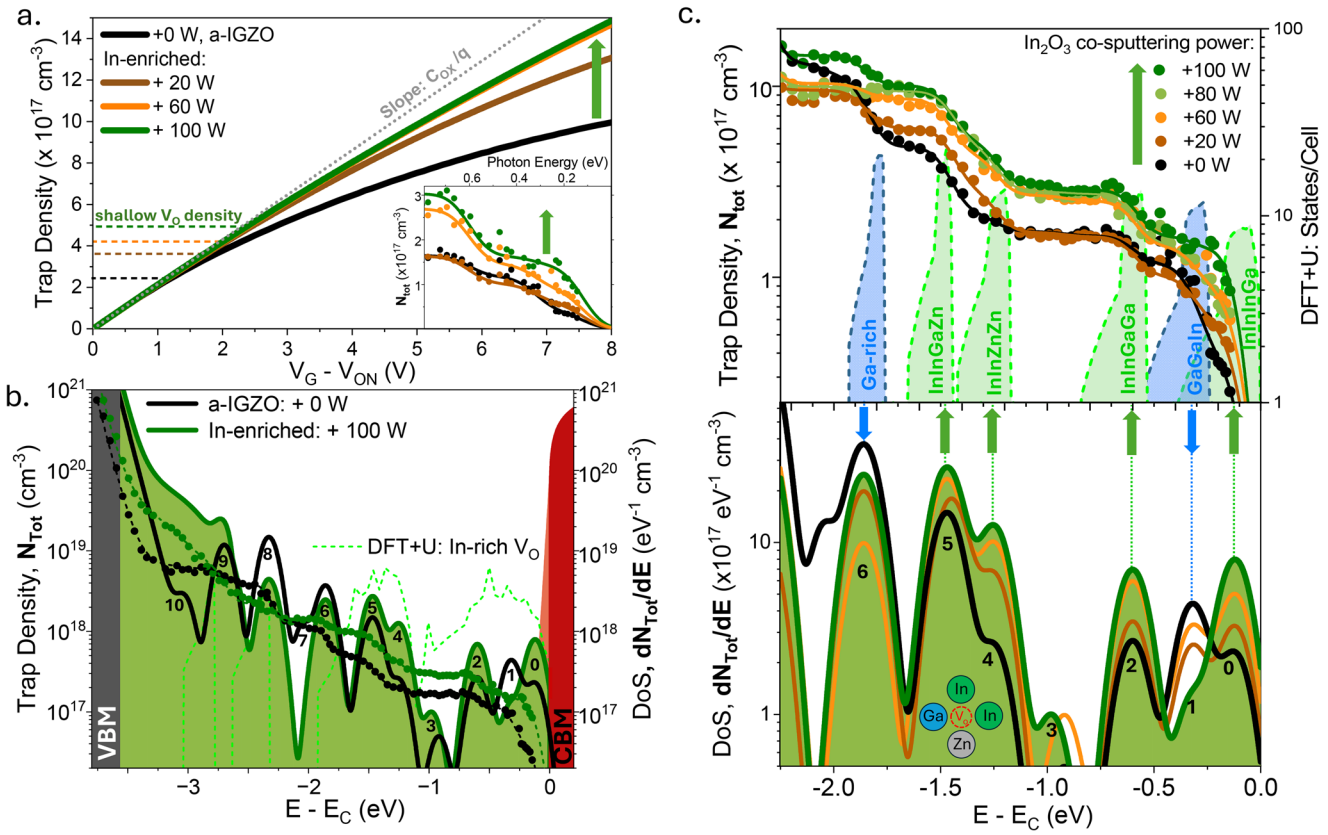


FIGURE 8 | (a) Extracted trap densities versus overvoltage curves for indium-enriched a-IGZO TFTs. (b) UP-DoS trap density (dots) and corresponding DoS (filled lines) for an a-IGZO (black) and an In-rich a-IGZO (dark green) TFT. DFT+U simulated DoS for oxygen vacancies with In-rich cation coordination environments (light green). (c) UP-DoS trap density (upper panel) and corresponding DoS (lower panel) of a-IGZO TFTs with increasing indium enrichment. DFT+U proposed oxygen vacancy cation coordination identifications are also indicated in the upper panel and matched to experimental DoS peaks.

transfer curve without any adjustable parameters. Simulating the entire TFT transfer curve requires only a single adjustable parameter: the conduction band tail Urbach energy. Alternatively, the shallow trap DoS responsible for subthreshold TFT behavior can instead be extracted from a TFT transfer curve and independently agree with trap density trends measured directly by UP-DoS.

An indium-enrichment study of a-IGZO TFTs fabricated via co-sputtering, in conjunction with DFT+U simulations, supports the proposal of specific cation coordination for the 11 oxygen-vacancy peaks observed in the UP-DoS. In conventional 1:1:1-ratio a-IGZO TFTs, the dominant shallow trap state that determines TFT performance is centered at ~0.32 eV below the conduction band mobility edge and is attributed to a Ga-Ga-In metal-coordinated oxygen vacancy. For an indium-rich a-IGZO TFT, a more shallow trap state appears at ~ 0.12 eV below the conduction band mobility edge and is attributed to an In–In–In–Ga or In–In–Zn metal-coordinated oxygen vacancy. Although indium enrichment of an amorphous oxide semiconductor is an attractive approach for achieving higher TFT mobility, due to a corresponding decrease in the electron effective mass, process optimization of such devices likely challenging. This challenge arises from the need to suppress shallow In-rich oxygen-vacancy defect states that accompany such indium enrichment.

4 | Experimental Section

4.1 | Preparation of a-IGZO TFTs

A diverse selection of a-IGZO TFTs is prepared for robust demonstration of how well UP-DoS simulates transfer curves that include: (1) back-gated TFTs from designs appropriate for display panel applications, (2) nanoscale dimension top-gated TFTs for DRAM memory application developments, and (3) back-gated TFTs with systematic In-enrichment. More specific details are available in Figure S1 and Tables S1, S2 and S3.

4.2 | Ultrabroadband Photoconduction Density of States (UP-DoS) Microscopy of a-IGZO TFTs

The integrated trap density, N_{tot}, of a-IGZO TFTs is measured using Ultrabroadband Photoconduction Density of States (UP-DoS) microscopy that has been modified to selectively excite shallow subgap defects within 0.14 eV of the conduction band mobility edge [48]. The inset of Figure 2 displays a rough schematic of the UP-DoS setup where the incident laser directly illuminates the TFT active channel using a reflective objective (52x, NA = 0.65) to create a near-diffraction-limited laser spot. Multiple tunable femtosecond lasers are coupled into the UP-DoS microscope via a home-built 4f-confocal piezo-scanning mirror

16163028, 0, Downloaded from https://advanced.onlinelibrary.wiley.com/doi/10.1002/adfm.78029 by Matt Graham - Oregon State University , Wiley Online Library on [02/09/2026]. See the Terms and Conditions (https://onlinelibrary.wiley.com/terms-and-conditions) on Wiley Online Library for rules of use; OA articles are governed by the applicable Creative Commons License

setup that enables continuous, selective laser excitation of subgap defect states. Collectively, the UP-DoS setup achieves full spectral (0.14–5 eV) and spatial resolution of the photon-normalized TFT photoconductance response (see Figure S5) [28, 48].

In UP-DoS, the UV–visible range is covered using a Ti: Sapphire laser with a harmonics extender (Coherent Chameleon Ultra II and APE Harmonix), and the near-IR (0.3–1.2 eV) range is covered using an automated optical parametric oscillator (OPO, APE Compact). Finally, this work enables a direct probe of shallow defect states near the conduction band mobility edge. This innovation is achieved through home-built difference-frequency generation (DFG) mixing of the OPO signal and idler laser lines on a $HgGa_2S_4$ nonlinear crystal, which provides tunable IR-laser energies down to ~0.1 eV [49].

The UP-DoS microscopy method employs a lock-in amplifier (Zurich MFLI) with a 585 Hz optical chopper frequency (Thorlabs MC2000B) to enhance the signal-to-noise ratio and largely remove transfer-curve drift effects that may otherwise affect the measured TFT photoconductance. Collection is via RF-probes in series with a current preamplifier (Femto DDPCA-300) at a fixed positive bias. The photoconduction signal is per-photon normalized, such that $I_{\mathrm{norm}}(h\nu) = h\nu I_{PC}/P$, where I_{PC} is the recorded increase in conduction due to the incident light and P is the incident power (nW to μW regime). UP-DoS is conducted at a fixed gate voltage with the TFT turned on and operating in the linear regime. Under these approximations, the TFT photoconduction is proportional to the number of carriers excited from the defect state to the conduction band by the equation [28, 50]:

$$N_{tot}(h\nu) = I_{\mathrm{norm}}(h\nu)\left[\frac{C_{ox}k_0}{qd}\left(\frac{\partial I_D}{\partial V_G}\right)^{-1}\right] \quad (1)$$

where $k_0 = \frac{P_{sat}}{h\nu_{E_g}}$ is the power saturation constant, $\frac{\partial I_D}{\partial V_G}$ is the transfer curve slope and d is the accumulation layer thickness. For subgap photoconduction in n-type TFTs, the photoconduction response $I_{\mathrm{norm}}(h\nu)$ reflects optical excitation from all filled trap states within an energy $h\nu$ of the conduction band minimum. As such, the raw UP-DoS spectrum, $I_{\mathrm{norm}}(h\nu)$ is directly proportional to the trap density, $N_{tot}(h\nu)$, and in turn the subgap DoS as $\mathrm{DoS}(E_C - E) = \frac{dN_{tot}(h\nu)}{dh\nu}$. Since the smoothing involved in numerical derivatives can be subjective, as shown in Figure 2a, the subgap DoS is instead retrieved by fitting $N_{tot}(h\nu)$ to a sequence of error functions, each offset by the defect energy, to match the expected stepwise-decreasing photoconduction response [50]. This analysis approach is compared with numerical derivatives of the UP-DoS spectra obtained with minimal or no smoothing. This comparison, along with further experimental details, is provided in Figures S5, S6, and S7.

4.3 | Simulation of TFT Transfer Curves from Experimental DoS

The drift mobility of a-IGZO TFTs is simulated from experimentally measured DoS by Fermi-Dirac statistics. The trapped and free charge sheet densities, induced by an applied gate voltage, $Q(F_n)$ and $Q_T(F_n)$, are evaluated as a function of the electron quasi-Fermi energy level, F_n [34]. Once $Q(F_n)$ and $Q_T(F_n)$ are known, the simulated drift mobility, $\mu_{SIM}(F_n)$ is calculated as [34, 40]:

$$\mu_{SIM}(F_n) = \mu_0\left(\frac{Q(F_n)}{Q(F_n) + Q_T(F_n)}\right) \quad (2)$$

where μ_0 is the trap-free extended state mobility. All simulations assume a $\mu_0 = 23\ \mathrm{cm}^2\ V^{-1}\ s^{-1}$, which is extracted from a best fit to Equation (2) of the empirical mobility data of Figure 2b and is consistent with previous literature estimates [34, 51–53] Note the trapped and free carrier densities are simply $n_T = Q_T/q$ and $n = Q/q$, where each electron has a charge of q. To relate the quasi-Fermi energy level, F_n, to the specific applied gate voltage, V_G, the charge sheet approximation, $C_{ox}(V_G - V_{ON}) = Q(F_n) + Q_T(F_n)$, is used to plot the DoS and related simulated quantities on a V_G axis (e.g., see Figures 1b and 4b–d) [34].

To convert simulated drift mobility, $\mu_{SIM}(V_G)$, to a corresponding simulated TFT source-drain current, the following EKV drain-current model is used [54]:

$$I_{D,SIM} = \mu_{SIM} \times 2\left(\frac{k_BT}{q}\right)^2 C_{ox}\frac{W}{L}\left\{\left[\ln\left(1+\exp\left(\frac{q(V_G - V_{ON})}{2k_BT}\right)\right)\right]^2 - \left[\ln\left(1+\exp\left(\frac{q(V_G - V_{ON} - V_D)}{2k_BT}\right)\right)\right]^2\right\} \quad (3)$$

The above equation is further used to extract an experimental TFT drift mobility, μ_{EKV}, directly from a transfer curve by setting the I_D factor equal to the experimentally measured source-drain current and subsequently solving for the mobility factor [34, 55]. To convert from $\mu_{EKV}(V_G)$ to the experimental free and trapped charge density induced by the applied gate voltage, we again employ the charge-sheet approximation to obtain [55],

$$Q_T(V_G) = C_{ox}(V_G - V_{ON})\left[1 - \frac{\mu_{\mathrm{EKV}}(V_G)}{\mu_0}\right] \quad (4)$$

$$Q(V_G) = C_{ox}(V_G - V_{ON})\left[\frac{\mu_{\mathrm{EKV}}(V_G)}{\mu_0}\right] \quad (5)$$

where μ_{EKV} is experimentally extracted drift mobility from the transfer curve and μ_0 is the same free extended state mobility of 23 $\mathrm{cm}^2\ \mathrm{V}^{-1}\ \mathrm{s}^{-1}$. While the extracted trap density at large gate overvoltages is strongly dependent on the assumed value of μ_0, the extracted shallow trap density at $V_G \approx V_T$, corresponding to the Gaussian-shaped shallow states, remains largely independent of the assumed μ_0 value (see Figure S12).

In the density of states simulation, the off-state quasi-Fermi energy level, at which $V_G = V_{ON}$, is set such that the simulated $Q(F_n) = Q(V_G = V_{ON})$ equals the extracted free charge density at $V_G = V_{ON}$ by Equation (5). This off-state quasi-Fermi level marks the boundary beyond which deeper states have negligible influence on gate voltage-induced electron trapping and is positioned ≈ 0.65 eV below the conduction band mobility edge. For TFT simulation purposes, the absolute scaling of the measured density

16163028, 0, Downloaded from https://advanced.onlinelibrary.wiley.com/doi/10.1002/adfm.78029 by Mart Graham - Oregon State University , Wiley Online Library on [02/09/2026]. See the Terms and Conditions (https://onlinelibrary.wiley.com/terms-and-conditions) on Wiley Online Library for rules of use; OA articles are governed by the applicable Creative Commons License

of states is initially treated as an adjustable parameter, while the relative scaling between different TFTs remains fixed and is held constant. For more details of the TFT simulations, together with a full list of equations and Fermi-Dirac statistics used, please refer to Figures S9, S10, S11, S12, and S13 and Table S5.

4.4 | DFT+U Defect Simulations

The DFT+U methods employed a multi-stage approach that began by placing 20 formula units of IGZO randomly into a cubic lattice cell with a volume 1.3 times that of the IGZO crystal structure. This was proceeded by taking the randomized cubic cell through a melt and quench process by employing the general lattice utility program (GULP), similar to previous simulation studies [28, 56, 57]. The quenched amorphous structures were further refined using Vienna ab initio Simulation Package (VASP) using the Perdew–Burke–Ernzerhof (PBE) generalized gradient approximation (GGA) functional theory, which resulted in amorphous IGZO structures with an approximate density of ~6.1 g/cm^3 that is consistent with results reported by Kamiya et al. [58–63] To introduce an oxygen vacancy to the amorphous structure, a single oxygen atom is randomly removed before the cell is relaxed. The local coordination environment of each simulated oxygen vacancy is defined as the set of atoms within 2.5 Å of the removed oxygen atom. More detailed information on the DFT+U simulation, including the cell-relaxation approach and scissoring method, is provided in Figures S3, S4, S15, and S16.

Acknowledgments

This work was supported by the SAMSUNG Global Research Outreach (GRO) Award and partly by Samsung Electronics Co., Ltd. (IO250414-12603-02) and a NSF Grant (DMR-1920368). Development of In-enriched TFTs in this work was supported by the Technology Innovation Program (RS-2025-02304448) funded by the Ministry of Trade, Industry & Energy (MOTIE, Korea), and by ANCHOR through the Seoul ANCHOR Center, funded by the Ministry of Education (MOE) and the Seoul Metropolitan Government. (2026-ANCHOR-01-022-04).

Conflicts of Interest

M.M., K.V. and M.G. are named inventors on a U.S. patent application (US 2025/0102448 A1) covering aspects of the ultrabroadband photoconduction methodology described in this work, which is assigned to Oregon State University.

Data Availability Statement

The data that support the findings of this study are available from the corresponding author upon request.

References

1. K. Nomura, H. Ohta, A. Takagi, T. Kamiya, M. Hirano, and H. Hosono, "Room-Temperature Fabrication of Transparent Flexible Thin-Film Transistors Using Amorphous Oxide Semiconductors," *Nature* 432, no. 7016 (2004): 488–492.

2. D. Geng, K. Wang, L. Li, et al., "Thin-Film Transistors for Large-Area Electronics," *Nature Electronics* 6, no. 12 (2023): 963–972.

3. T. Kamiya, K. Nomura, and H. Hosono, "Present Status of Amorphous In–Ga–Zn–O Thin-Film Transistors," *Science and Technology of Advanced Materials* (2010): 044305.

4. B. Bao, J. Xie, T. Xia, et al., "Amorphous IGZO Thin-Film Transistors: Materials, Device Structures, Fabrications, and Application Explorations," *Advanced Functional Materials* 35, no. 41 (2025): 2503755.

5. F. Liao, Z. Zhu, Z. Li, et al., "High-Density Three-Dimensional Integration of Dynamic Random-Access Memory Using Vertical Dual-Gate IGZO TFTs," *Nature Communications* 16, no. 1 (2025): 10932.

6. S. Ryu, M. Kang, K. Cho, and S. Kim, "Capacitorless Two-Transistor Dynamic Random-Access Memory Cells Comprising Amorphous Indium–Tin–Gallium–Zinc Oxide Thin-Film Transistors for the Multiply–Accumulate Operation," *Advanced Materials Technologies* 9, no. 15 (2024): 2302209.

7. D. Ha, Y. Lee, S. Yoo, et al., "Exploring Innovative IGZO-Channel-Based DRAM Cell Architectures and Key Technologies for Sub-10 nm Nodes," in *2024 Institute of Electrical and Electronics Engineers International Memory Workshop (IMW)* (IEEE, 2024), 1–4.

8. Y. Jang, J. Park, J. Kang, and S.-Y. Lee, "Amorphous InGaZnO (a-IGZO) Synaptic Transistor for Neuromorphic Computing," *ACS Applied Electronic Materials* 4, no. 4 (2022): 1427–1448.

9. Y. Yun, J. Park, M. Kong, et al., "Optoelectronic Neuromorphic System Based on Amorphous Indium–Gallium–Zinc–Oxide Thin-Film Transistor for Spiking Neural Networks," *Advanced Intelligent Systems* 8 (2025): 2500402.

10. J. Chung, K. Park, G. I. Kim, et al., "Visible Light-Driven Indium–Gallium–Zinc–Oxide Optoelectronic Synaptic Transistor with Defect Engineering for Neuromorphic Computing System and Artificial Intelligence," *Applied Surface Science* 610 (2023): 155532.

11. G. W. Mattson, K. T. Vogt, J. F. Wager, and M. W. Graham, "Illuminating Trap Density Trends in Amorphous Oxide Semiconductors with Ultrabroadband Photoconduction," *Advanced Functional Materials* 33, no. 25 (2023): 2300742.

12. H. Hong, M. J. Kim, D.-J. Yi, et al., "Quantitative Analysis of Defect States in InGaZnO within 2 eV below the Conduction Band via Photo-Induced Current Transient Spectroscopy," *Scientific Reports* 13, no. 1 (2023): 13407.

13. K. Ide, Y. Kikuchi, K. Nomura, M. Kimura, T. Kamiya, and H. Hosono, "Effects of Excess Oxygen on Operation Characteristics of Amorphous In-Ga-Zn-O Thin-Film Transistors," *Applied Physics Letters* 99, no. 9 (2011): 986998.

14. S. Mao, G. Wang, and C. Zhao, "Amorphous Oxide Semiconductor for Monolithic 3D DRAM: An Enabler or Passer-By?," *National Science Review* 11, no. 3 (2024): nwad290.

15. S. Yan, Z. Cong, N. Lu, J. Yue, and Q. Luo, "Recent Progress in InGaZnO FETs for High-Density 2T0C DRAM Applications," *Science China Information Sciences* 66, no. 10 (2023): 200404.

16. J. F. Wager, B. Yeh, R. L. Hoffman, and D. A. Keszler, "An Amorphous Oxide Semiconductor Thin-Film Transistor Route to Oxide Electronics," *Current Opinion in Solid State and Materials Science* 18, no. 2 (2014): 53–61.

17. Y. Zhu, Y. He, S. Jiang, L. Zhu, C. Chen, and Q. Wan, "Indium–Gallium–Zinc–Oxide Thin-Film Transistors: Materials, Devices, and Applications," *Journal of Semiconductors* 42, no. 3 (2021): 031101.

18. Q. Hu, C. Gu, Q. Li, et al., "True Nonvolatile High-Speed DRAM Cells Using Tailored Ultrathin IGZO," *Advanced Materials* 35, no. 20 (2023): 2210554.

19. R. W. Keyes, "Physical Limits of Silicon Transistors and Circuits," *Reports on Progress in Physics* 68, no. 12 (2005): 2701.

20. J. S. Hur, S. Lee, J. Moon, et al., "Oxide and 2D TMD Semiconductors for 3D DRAM Cell Transistors," *Nanoscale Horizons* 9, no. 6 (2024): 934–945.

21. A. R. Choi, D. H. Lim, S.-Y. Shin, et al., "Review of Material Properties of Oxide Semiconductor Thin Films Grown by Atomic Layer Deposition for Next-Generation 3D Dynamic Random-Access Memory Devices," *Chemistry of Materials* 36, no. 5 (2024): 2194–2219.

16163028, 0, Downloaded from https://advanced.onlinelibrary.wiley.com/doi/10.1002/adfm.78029 by Mart Graham - Oregon State University , Wiley Online Library on [02/09/2026]. See the Terms and Conditions (https://onlinelibrary.wiley.com/terms-and-conditions) on Wiley Online Library for rules of use; OA articles are governed by the applicable Creative Commons License

22. T. Kamiya, K. Nomura, and H. Hosono, "Electronic Structure of the Amorphous Oxide Semiconductor a-InGaZnO4–x: Tauc–Lorentz Optical Model and Origins of Subgap States," *Physica Status Solidi A: Applications and Materials Science* 206, no. 5 (2009): 860–867.

23. A. D. J. De Meux, G. Pourtois, J. Genoe, and P. Heremans, "Comparison of the Electronic Structure of Amorphous versus Crystalline Indium Gallium Zinc Oxide Semiconductor: Structure, Tail States and Strain Effects," *Journal of Physics D: Applied Physics* 48, no. 43 (2015): 435104.

24. T.-C. Fung, C.-S. Chuang, C. Chen, et al., "Two-Dimensional Numerical Simulation of Radio Frequency Sputter Amorphous In–Ga–Zn–O Thin-Film Transistors," *Journal of Applied Physics* 106, no. 8 (2009): 084511.

25. S. Lee, J. Lee, M. Lee, et al., "High-Performance Oxide Semiconductor TFT with a-IGZO/In-Rich a-IGZO Heterostructure Using Quantum Confinement Effects: Enhancing Mobility and Reliability," *Journal of Alloys and Compounds* 1036 (2025): 182035.

26. H. Cho, M. Tsuji, S. Ueda, J. Kim, and H. Hosono, "Oxygen Defects and Instability in Very Thin a-IGZO TFTs," *Advanced Electronic Materials* 11, no. 15 (2025): e00349.

27. L. S. R. Kumara, K. Ishikawa, K. Ide, H. Hosono, T. Kamiya, and O. Sakata, "Local Structure Properties of Hydrogenated and Non-hydrogenated Amorphous In–Ga–Zn–O Thin Films Using XAFS and High-Energy XRD," *The Journal of Physical Chemistry C* 125, no. 24 (2021): 13619–13628.

28. K. T. Vogt, C. E. Malmberg, J. C. Buchanan, et al., "Ultrabroadband Density of States of Amorphous In-Ga-Zn-O," *Physical Review Research* 2, no. 3 (2020): 033358.

29. J. Yoo, H. S. Jo, S.-B. Jeon, et al., "Direct Observation for Distinct Behaviors of Gamma-Ray Irradiation-Induced Subgap Density-of-States in Amorphous InGaZnO TFTs by Multiple-Wavelength Light Source," *Advanced Electronic Materials* 10, no. 8 (2024): 2300906.

30. R. Nakazawa, A. Matsuzaki, K. Shimizu, et al., "In-Gap States of an Amorphous In–Ga–Zn–O Thin Film Studied via High-Sensitivity Ultraviolet Photoemission Spectroscopy Using Low-Energy Photons," *Applied Physics Express* 14, no. 7 (2021): 071004.

31. L. Zheng, L. Xing, Z. Lin, et al., "Are There High-Density Deep States in an Atomic-Layer-Deposited Indium–Gallium–Zinc Oxide Thin Film?," *Nano Letters* 25, no. 14 (2025): 5974–5980.

32. A. de Jamblinne de Meux, A. Bhoolokam, G. Pourtois, J. Genoe, and P. Heremans, "Oxygen Vacancy Effects in a-IGZO: Formation Mechanisms, Hysteresis, and Negative Bias Stress Effects," *Physica Status Solidi A* 214, no. 6 (2017): 1600889.

33. H. Hosono, "Transparent Amorphous Oxide Semiconductors for Display Applications: Materials, Features, Progress, and Prospects," in *Amorphous Oxide Semiconductors: IGZO and Related Materials for Display and Memory*, (John Wiley & Sons, 2022): 1–20.

34. J. F. Wager, "Amorphous Semiconductor Mobility Physics and TFT Modeling," in *Amorphous Oxide Semiconductors: IGZO and Related Materials for Display and Memory*, (John Wiley & Sons, 2022), 105–123.

35. H.-W. Yeon, S.-M. Lim, J.-K. Jung, et al., "Structural-Relaxation-Driven Electron Doping of Amorphous Oxide Semiconductors by Increasing the Concentration of Oxygen Vacancies in Shallow-Donor States," *NPG Asia Materials* 8, no. 3 (2016): e250–e250.

36. Y.-G. Park, D. Y. Cho, R. Kim, et al., "Defect Engineering for High Performance and Extremely Reliable a-IGZO Thin-Film Transistor in QD-OLED," *Advanced Electronic Materials* 8, no. 7 (2022): 2101273.

37. R. Nakazawa, A. Matsuzaki, K. Shimizu, et al., "Reliable Measurement of the Density of States Including Occupied in-Gap States of an Amorphous In–Ga–Zn–O Thin Film via Photoemission Spectroscopies: Direct Observation of Light-Induced in-Gap States," *Journal of Applied Physics* 135, no. 8 (2024): 085301.

38. G. W. Mattson, K. T. Vogt, J. F. Wager, and M. W. Graham, "Hydrogen Incorporation into Amorphous Indium Gallium Zinc Oxide Thin-Film Transistors," *Journal of Applied Physics* 131, no. 10 (2022): 2836711.

39. M. Kimura, K. Ide, K.-J. Zhou, et al., "Tandem Neural Network Rapidly Solves Multivalued Inverse Problems: Application to Oxide-Semiconductor Characterization," *Advanced Intelligent Systems* 8 (2026): e70437.

40. A. Nenashev, J. Oelerich, S. Greiner, A. Dvurechenskii, F. Gebhard, and S. Baranovskii, "Percolation Description of Charge Transport in Amorphous Oxide Semiconductors," *Physical Review B* 100, no. 12 (2019): 125202.

41. S. Kim, Y. Lee, S. Shin, et al., "Mobility Overestimation in Thin-Film Transistors: Effects of Device Geometry and Fringe Currents," *ACS Nano* 19, no. 41 (2025): 36614–36625.

42. N. F. Mott and E. A. Davis, *Electronic Processes in Non-Crystalline Materials* (OUP Oxford, 2012).

43. J. Klein, L. Kampermann, B. Mockenhaupt, M. Behrens, J. Strunk, and G. Bacher, "Limitations of the Tauc Plot Method," *Advanced Functional Materials* 33, no. 47 (2023): 2304523.

44. X. Chen, G. He, J. Gao, et al., "Substrate Temperature-Dependent Structural, Optical and Electrical Properties of Amorphous InGaZnO Thin Films," *Journal of Alloys and Compounds* 632 (2015): 533–539.

45. Q. Shangguan, Y. Lv, and C. Jiang, "A Review of Wide Bandgap Semiconductors: Insights into SiC, IGZO, and Their Defect Characteristics," *Nanomaterials* 14, no. 20 (2024): 1679.

46. P. King, T. D. Veal, F. Fuchs, et al., "Band Gap, Electronic Structure, and Surface Electron Accumulation of Cubic and Rhombohedral In_2O_3," *Physical Review B—Condensed Matter and Materials Physics* 79, no. 20 (2009): 205211.

47. O. Bierwagen, "Indium Oxide—A Transparent, Wide-Band Gap Semiconductor for (Opto)electronic Applications," *Semiconductor Science and Technology* 30, no. 2 (2015): 024001.

48. K. T. Vogt, M. Mattsson, and M. W. Graham, "Ultrabroadband Photoconduction Method and Apparatus for Defect Density of States Microscopy in Semiconductor Devices," *US Patent Application US2025102448A1* (2025), Filed by Oregon State University. United States Patent and Trademark Office.

49. M. Beutler, I. Rimke, E. Büttner, V. Badikov, and V. Petrov, "Femtosecond Mid-IR Difference-Frequency Generation in $HgGa_2S_4$ from an 80 MHz Optical Parametric Oscillator Pumped at 800 nm," *Journal of the Optical Society of America B* 33, no. 11 (2016): D7–D11.

50. M. J. Mattsson, K. M. Niang, J. Parker, et al., "Defect Density of States of Tin Oxide and Copper Oxide P-Type Thin-Film Transistors," *Advanced Electronic Materials* 11, no. 11 (2025): 2400929.

51. I. I. Fishchuk, A. Kadashchuk, A. Bhoolokam, et al., "Interplay Between Hopping and Band Transport in High-Mobility Disordered Semiconductors at Large Carrier Concentrations: The Case of the Amorphous Oxide InGaZnO," *Physical Review B* 93, no. 19 (2016): 195204.

52. K. A. Stewart, B.-S. Yeh, and J. F. Wager, "Amorphous Semiconductor Mobility Limits," *Journal of Non-Crystalline Solids* 432 (2016): 196–199.

53. K. A. Stewart and J. F. Wager, "Thin-Film Transistor Mobility Limits Considerations," *Journal of the Society for Information Display* 24, no. 6 (2016): 386–393.

54. C. C. Enz, F. Krummenacher, and E. A. Vittoz, "An Analytical MOS Transistor Model Valid in All Regions of Operation and Dedicated to Low-Voltage and Low-Current Applications," *Analog Integrated Circuits and Signal Processing* 8, no. 1 (1995): 83–114.

55. J. F. Wager, "Thin-Film Transistor Accumulation-Mode Modeling," *Solid-State Electronics* 197 (2022): 108424.

56. J. D. Gale *Journal of the Chemical Society, Faraday Transactions* 93 (1997): 629.

16163028, 0, Downloaded from https://advanced.onlinelibrary.wiley.com/doi/10.1002/adfm.78029 by Matt Graham - Oregon State University , Wiley Online Library on [02/09/2026]. See the Terms and Conditions (https://onlinelibrary.wiley.com/terms-and-conditions) on Wiley Online Library for rules of use; OA articles are governed by the applicable Creative Commons License

57. J. C. Buchanan, D. B. Fast, B. E. Hanken, et al., "Structural Convergence Properties of Amorphous $InGaZnO_4$ from Simulated Liquid-Quench Methods," *Dalton Transactions* 46 (2017): 15311.

58. T. Kamiya, K. Nomura, and H. Hosono, "Present Status of Amorphous In-Ga-Zn-O Thin-Film Transistors," *Science and Technology of Advanced Materials* 11 (2010): 044305.

59. G. Kresse and J. Furthmüller, "Efficiency of ab-initio Total Energy Calculations for Metals and Semiconductors Using a Plane-Wave Basis Set," *Computational Materials Science* 6, no. 1 (1996): 15–50.

60. G. Kresse and J. Furthmüller, "Efficient Iterative Schemes for ab initio Total-Energy Calculations Using a Plane-Wave Basis Set," *Physical Review B* 54, no. 16 (1996): 11169.

61. G. Kresse and D. Joubert, "From Ultrasoft Pseudopotentials to the Projector Augmented-Wave Method," *Physical Review b* 59, no. 3 (1999): 1758.

62. J. P. Perdew, K. Burke, and M. Ernzerhof, "Generalized Gradient Approximation Made Simple," *Physical Review Letters* 77, no. 18 (1996): 3865.

63. G. Kresse and J. Hafner, "Ab initio Hellmann-Feynman Molecular Dynamics for Liquid Metals," *Journal of Non-Crystalline Solids* 156 (1993): 956–960.

Supporting Information

Additional supporting information can be found online in the Supporting Information section.

Supporting File: adfm78029-sup-0001-SuppMat.pdf.

16163028, 0, Downloaded from https://advanced.onlinelibrary.wiley.com/doi/10.1002/adfm.78029 by Mart Graham - Oregon State University , Wiley Online Library on [02/09/2026]. See the Terms and Conditions (https://onlinelibrary.wiley.com/terms-and-conditions) on Wiley Online Library for rules of use; OA articles are governed by the applicable Creative Commons License